HYBRID LARGE EDDY SIMULATIONS OF AN UNCOOLED HIGH PRESSURE TURBINE STATOR-ROTOR STAGE

James Kopriva – Gregory M. Laskowski

GE Aviation, Lynn MA, USA 01905

ABSTRACT

Turbulence plays an important role on the aero-thermal performance of modern aircraft engine high pressure turbines. The role of the vane wake and passage turbulence on the downstream blade is an important consideration for both performance and durability. In this paper, we consider turbulence and transition modeling for RANS, hybrid RANS/LES and wall resolved LES simulations of a span-wise periodic representation of the uncooled vane of Arts and Rouvroit geometry to establish predictive capability. A fundamental blade has been designed to pair with the uncooled vane to evaluate the impact of passage turbulence and vane wake on the downstream blade boundary layer, wake formation and evolution. Finally, the learnings from the statistical 2D simulations are applied to a full 3D annular representation of the geometry to demonstrate impact of secondary flows on the overall aero-thermal performance of the stage.

KEYWORDS

HIGH PRESSURE TURBINE, CFD, UNSTEADY FLOW, TURBULENCE

NOMENCLATURE

AX	Axial Chord
C	Chord
CFD	Computational Fluid Dynamics
h	Heat Transfer Coefficient
HLES	Hybrid Large Eddy Simulation
HPT	High Pressure Turbine
LE	Vane or Blade Leading-edge
L_e	Dissipation Length Scale
L_I	Integral Length Scale
LES	Large Eddy Simulation
Ma	Mach Number
Nu	Nusselt Number
p	Pitch
Pt	Total Pressure
Ptr	Relative Total Pressure
RANS	Reynolds Averaged Navier-Stokes Equations
Re	Reynolds Number
s	Surface Distance
TI	Turbulence Intensity
1, 2, 3	Vane Inlet, Inter-stage, and Blade Exit Plane Locations
$\Delta s+$	First Cell Stream-wise Distance in Wall Units, $\rho s\mu_\tau/\mu$
$\Delta y+$	First Cell Wall Normal Height in Wall Units, $\rho y\mu_\tau/\mu$
$\Delta z+$	First Cell Span-wise Distance in Wall Units, $\rho z\mu_\tau/\mu$
ω	Specific Turbulence Dissipation Rates

INTRODUCTION

Computational Fluid Dynamics is an indispensable tool for the design of high pressure turbine components, but limitations of turbulence modeling for accuracy (RANS) or speed (LES) are well documented (Laskowski et al., 2015, Slotnick et al., 2014). Hybrid turbulence modeling methods, which attempt to find a compromised between the two methods, have the potential to become viable for design iterations as the methods mature and computer hardware technology continues to advance.

RANS methods have seen success for fully turbulent attached flows (Claus et al. 2006) however, the well-known limitations of RANS methods for separated flows restrict their use to a limited design space (Tinoco et al., 2005). More precisely, modeling challenges include smooth body separation for high-speed stall, low-speed high-lift, compressor stall, turbulence migration, and impact on momentum and enthalpy mixing through the HPT (Laskowski et al., 2016, Kopriva et al., 2013). These examples require the accurate prediction of regions of wakes, flow separation, and/or boundary layer transition. Slotnick et al. (2014) states the current most critical item and likely pacing item for 2030 is the ability to adequately predict turbulent flows with possible boundary layer transition and flow separation present. Fortunately, in the advent of supercomputing, LES can play a key role in maturing the physical understanding of these complex flow fields. Although LES can accurately predict the desired flow regimes (wakes, flow separation, and boundary layer transition), industrial applications still require a lower computation cost approach. In order for RANS models to better capture boundary layer transition, purely empirical two equation transition models have been derived (Stock and Haase, 2006, Menter et al., 2006). Each model requires a level of empiricism; therefore, the turbulence model is dependent on the data set used to calibrate it. Hybrid unsteady RANS/LES methods provide improved predictive capability for wakes and other regions of separated flows at a lower computational cost than LES.

Hybrid models evoke RANS or wall modeled (WM) LES near the wall, lowering the grid requirement and therefore computational cost. This also allows for the use of RANS based transition models; however, the integration of transition modeling with hybrid models has not been well vetted (Slotnick et al., 2014). The significant benefit of the hybrid models is the employment of LES in regions of separation for improved accuracy. It should be noted that for hybrid methods to be routinely used, a fluid RANS-to-LES transition in the boundary layer is required. Wall resolved LES can play a key role in assessing regions of boundary layer transition and flow separation which will be addressed in this paper.

The high pressure turbine is typically subject to very high heat loads, high levels of turbulence, and significant unsteadiness due to moving blade rows. The state of the boundary layer plays a direct role both in heat transfer as well as wake formation, evolution and decay. Mayle (1991) and later Walker (1993) provide an extensive overview of the role of transition in turbomachinery flows. Radomsky and Thole (2002) conducted LDV measurements of a smooth, uncooled turbine vane at engine relevant Re and Ma for 0.6% and 20% freestream turbulence levels. The integral and dissipation length scale were $L_e/C=0.09$ and $L_l/C=0.21$ respectively for the 20% turbulence case. No turbulence spectrum or length scales were report for the 0.6% freestream turbulence case. The results show that for TI=0.6% the pressure side boundary layer remained laminar and the suction side boundary layer transitioned to turbulent just upstream of the trailing edge (TE). More interestingly, the results show a similar trend at TI=20%, with transition location moving upstream on the suction side surface. Similar observations were noted by Arts and Rouvroit (1992) for measured heat flux on a transonic uncooled airfoil at TI=0 and 6%. Kopriva et al. (2015) included the upstream bars used to generate the 6% turbulence level and showed agreement with both the turbulent decay and the frequency content with LES. Using Taylor hypothesis of frozen turbulence, based on the 1st harmonic frequency, the turbulent length scale of $L_l/C=0.16$ was found. Experimental test cases, where no upstream bars were present, the natural TI for the facility resulted in TI<1%. However, no frequency spectrum was provided for TI<1%. The study of Arts and Rouvroit (1992) has been the focus on numerous numerical studies including Bhaskaran (2010), Morata et al. (2013), Kopriva et al. (2013), Kopriva et al. (2014), and Kopriva et al. (2015).

The role of turbulence and unsteadiness on boundary layer and wakes for high pressure turbine blades is less well understood. Kopriva et al. (2014) designed a turbine blade based on the high pressure turbine vane described by Arts and Rouvroit (1992). In this paper, we provide a methodical simulation approach evaluating RANS, transition models, hybrid LES and LES starting with the uncooled vane of Arts and Rouvroit (1992). The 2D blade designed by Kopriva et al. (2014) is then included in the analysis leveraging lessons learned for grid resolution, time step and physics model from the vane analysis. Finally, hybrid LES with transition modeling is compared to RANS in order to gain further insight to the boundary layer and wake flow physics on an uncooled HPT 3D stator-rotor system.

APPROACH

Given the complexity of typical turbine designs, a robust solver and automated meshing is desired. Numerical schemes must be tolerant of complex geometry resulting in less than desirable mesh quality, while at the same time be capable of delivering accurate results. Modeling techniques must be robust enough to deliver converged solutions over a range of design conditions with minimal user intervention. Additionally, automated meshing for optimization is becoming more common for complex design features where unstructured meshing is required (Zlatinov and Laskowski, 2015).

The present study takes an industrial HPT modeling approach using the commercial solver Fluent and unstructured meshing using prism and tetrahedral elements. RANS, HLES, and LES approaches are evaluated against experimental measurement for the HPT vane of Arts and Rouvroit (1992). Each modeling approach will be assessed in its ability to capture boundary layer development and impact on wake formation. This understanding will be a critical building block before extending this study to vane/blade stage interaction to understand the impact of periodic unsteadiness on the downstream blade. A downstream blade has been designed by the authors and paired with the experimental measured vane of Arts and Rouvroit (1992), therefore anchoring additional computational studies to experimental data. This also ensures numerical and measurement comparisons are first understood before exploring increasing complex physics due to the coupled vane/blade interaction.

Computational results will be compared at $Re=1.16x10^6$ and Ma=0.84 where loading and wake profile were reported. This case is referred to as MUR129 by Arts and Rouvroit (1992) where the measured inlet TI of 0.8% was reported. The measured total pressure wake provides an opportunity to assess the impact of boundary layer development on mixing loss. The uncertainty reported by Arts and Rouvroit (1992) were based on a 20:1 confidence interval. The measurement uncertainties were ±0.5% for pressure, ±1.5% for temperature, ±5.0% for the heat transfer coefficient, and ±0.5 degrees on the exit flow angle. The current study computes the experiment uncertainty bars for both the vane surface Nusselt number and the downstream normalized total pressure wake. Total pressure wake uncertainty is based on reported wake to wake variation and measurement uncertainties.

Numerical Approach

LES, HLES, and RANS simulations are run using ANSYS Fluent v16. The unstructured grid consists of prism elements near the solid wall and tetrahedral elements in the core flow regions. Mesh cell maximum skewness was above 0.5. The total prism layer thickness is selected to meet maximum boundary layer thickness. For all computational cases the near wall Δy^+ remains under 1. Since an unstructured meshing approach is used, Δs^+ is approximately equal to Δz^+, where 250 and 50 are the peak values of RANS and LES, respectively. HLES uses the same near wall and core flow mesh resolution as RANS. The goal was not to optimize the RANS grid topology but rather to demonstrated how the model performed on a common mesh. For the pitch-line vane only studies, the total number of elements for RANS, HLES, and LES where 15, 15, and 55 million, respectively. The CPU hours relative to the LES simulation time was approximately 1/4 and 1/100 the CPU hours for HLES and RANS simulation. LES and HLES cases were advanced with a time step of dt=2x10-7 seconds. The simulations typically achieved statistical steady state after 12,000 time steps after which the solution was time averaged for another 12,000 iterations. This is equivalent to averaging over 4 vane flow through times from the LE to the TE of the vane. The Strouhal number of the vane wake based on simulation was found to be ~0.28 based on the TE thickness and exit velocity for the vane. This resulted in approximately 100 time step per shedding period.

Experimental data of Arts and Rouvroit (1992) is used to assess loading, surface heat transfer, and wake computational predictions. When expanding the study to include the interaction with a downstream blade a wall resolved WALE sub-grid scale LES model is used the assess RANS and HLES modeling approach. The WALE model is designed to return the correct wall asymptotic ($\sim y^3$) behavior for wall bounded flows. Another advantage is for laminar shear flows where a zero turbulent viscosity is returned. This allows the correct treatment of laminar zones in the domain (Nicoud and Ducros, 1999). HLES provides a computational cost savings due to the near wall mesh requirement. The IDDES model is selected for the hybrid approach where a “soft interface” blends RANS and LES regions. This allows for RANS treatment for near wall and steady flow regions and LES treatment of unsteady separated and shear flow regions. Improvements over the previous models were directed towards fixing the "log-layer mismatch" problem and a new definition of a sub-grid length scale that accounts for the near-wall distance (Shur et al., 2008). Additionally, given an unsteady inlet boundary condition, the IDDES model will operate in a WMLES mode

given that near wall mesh resolution is adequate. This capability is of particular interest for the blade in the downstream unsteady flow field of an upstream vane.

For RANS or HLES models to predict transitional boundary layers, Menter's γ-Re_θ transition model is coupled with the two-equation k-ω model with SST correction (Menter et al., 2009). The γ-Re_θ transition model was selected for its wide use in industrial flows, application for unstructured grids, and calibration to natural, bypass, and separated induced transition. There has been limited evaluation across all transition models in the area of "wake-induced" transition where the γ-Re_θ model will be assessed here. The authors acknowledge further model calibration work can still improve the model for roughness, free-stream turbulent length scale, streamline curvature, and "wake-induced" transition. However, it will be shown there is a substantial improvement in RANS and HLES predicts by including this transition model and a cost and accuracy opportunity in further developing transition modeling for HLES application. The cost reduction is due to the RANS near wall mesh target. Accuracy opportunity comes with the ability to capture the boundary layer state that will contribute to the development of the downstream wake mixing.

Second-order bounded central differencing scheme is applied for the spatial discretization of the momentum in WALE and IDDES calculations. The bounded central differencing scheme is based on the normalized variable diagram (NVD) approach (Leonard, 1991) along with convection boundedness criterion (CBC). The bounded central differencing scheme is a composite NVD-scheme that consists of a pure central differencing, a blended scheme of the central differencing, and the second-order upwind scheme. The same scheme is used for all other transport equations for the WALE calculations. IDDES modeling utilizes second-order upwind discretization scheme for all other transport equations. The second-order upwind discretization scheme is used for all transport equations for the SST RANS turbulence models. A bounded second-order implicit time advancement scheme is used for WALE and IDDES models.

Table 1: Modeling Selection.

RANS	SST turbulence model
RANS-T	SST with γ-Re_θ transition model
HLES-T	SST based IDDES with γ-Re_θ transition model
LES	WALE sub-grid scale model

Geometry and Setup

Figure 1 and 2 shows the vane only (VO), 2D linearly extruded sliding mesh (2DSM), and 3D sliding mesh (3DSM) domain. For the VO simulations, the computational domain exit is placed at X/C_{AX}=3.0 to allow the domain to include wake measurement plane at X/C_{AX}=1.44, where C_{AX} is based on the nozzle axial chord. Pitch-line experimental measurements were made on the linear cascade where the flow is assumed statistically two-dimensional due to the high span to chord vane aspect ratio of approximately 1.5. Therefore, computationally, both pitch and span-wise periodic boundary conditions are applied. The LES span-wise domain requirement was driven by the vane's TE vortex generation where computational span to true chord was set to 12%. This results in approximately 135 elements along the vane surface in the span-wise direction. This ensured a domain independent solution for HLES and LES predictions (Kopriva et al., 2014). Boundary conditions are provided for inlet total pressure and temperature where the flow enters normal in the domain inlet plane (See Table C3). Static pressure is provided at the domain exit plane. No-slip boundary conditions were specified at the vane wall with an isothermal wall temperature provided by Arts and Rouvroit (1992).

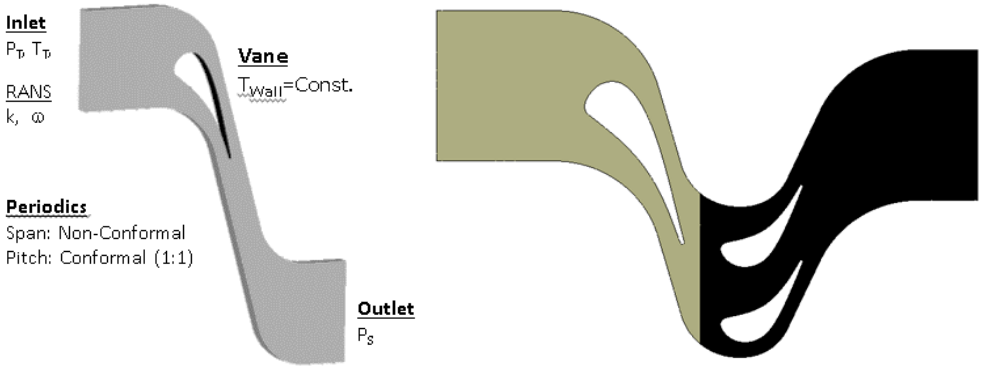

Figure 1: Vane only (left) and 2D sliding mesh (right) computational domain.

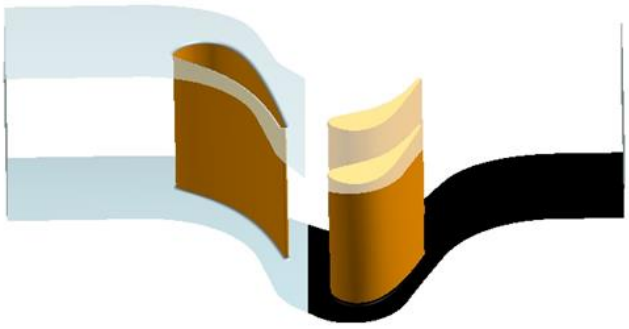

Figure 2: 3D sliding mesh (endwalls and blade tip clearance) computational domain.

When including the downstream blade, the stage pressure ratio is set to 2.35. The 2DSM maintains a linear passing blade speed of 250 m/s, where the 3DSM blade has an equivalent tangential speed at 50% span. The 2DSM vane and blade geometry are matched to the 50% span section of the 3DSM geometry. In addition, the stage design maintains the same vane pressure ratio to understand the role of unsteadiness and turbulence in the vane/blade interaction. Further details on the stage design are provided in the Appendix and Kopriva et al. (2014).

RESULTS

Figure 3 presents instantaneous numerical Schlieren for VO, 2DSM, and 3DSM for HLES-T. The simulations clearly show RANS-like steady flow behavior in the vane passage and LES-like unsteady scale resolved flow behavior in the wake of both the vane and the blade. The interaction of the vane wake with the suction side (SS) boundary layer is apparent for the particular time-step in the 2DSM and one objective of the present work is to better understand the resulting physics.

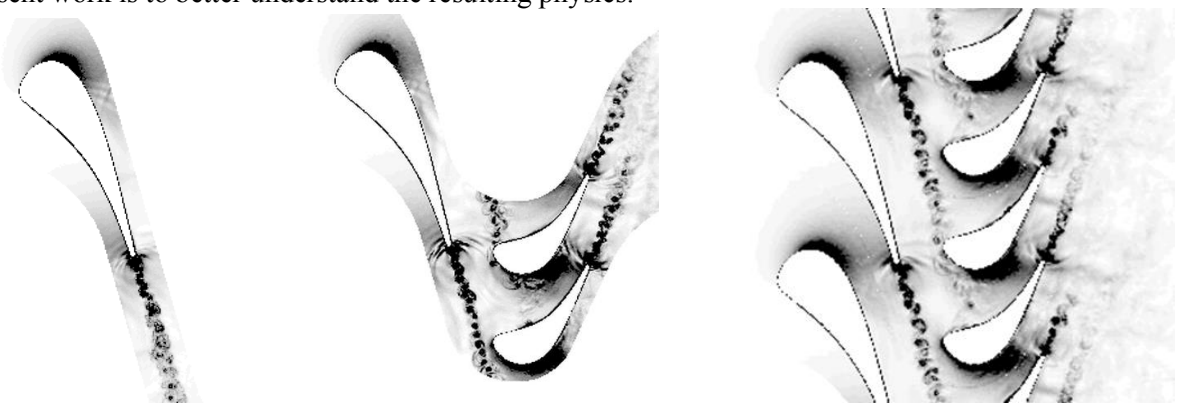

Figure 3: Numerical Schlieren at the pitchline for vane only (VO) left, 2D sliding mesh (2DSM) middle, and 3D sliding mesh (3DSM) right.

HPT Vane Only

The uncooled vane of Arts and Rouvroit (1992) serves as the foundation for the stator-rotor interaction problem. To gain confidence in the predictions, different turbulence modeling approaches are considered for the vane alone case. Simulations were conducted for RANS, RANS-T, HLES-T and WALE where surface heat flux is compare non-dimensionally by

$$\mathbf{Nu_C} = \mathbf{hC}/\mathbf{k} \qquad [1]$$

where

$$\mathbf{h} = \mathbf{q_{wall}}/(\mathbf{T_{t1}} - \mathbf{T_{wall}}) \qquad [2].$$

The wall temperature (T_{wall}) is constant and T_{t1} is the total temperature at the vane inlet based on the experimental results reported by Arts and Rouvroit (1992). Not surprisingly, the impact of the turbulence

model on the loading is negligible as shown in Figure 4a. The near wall mesh resolution, Δs^+ ($=\Delta z^+$), is shown in Figure 4b. Δs^+ is found to be equivalent between HLES-T and RANS-T until the TE region on the SS surface. This shows when TE shedding unsteadiness first impacts the IDDES model.

The low measured inlet TI of 0.8% was not modeled or resolved for HLES and LES simulation. This is supported by running the SST-T model at 0.8 and 0% inlet TI. Since no experimental spectral analysis was provided, a range of specific turbulence dissipation rates were also run corresponding to dissipation length scales (L_e=k/e) of 5, 0.5, and 0.05 based on the vane chord, L_e/C. The SST-T sensitivities are presented in Figure 5a and show a negligible impact on the surface Nu and SS transition.

The impact of the turbulence model on the heat transfer is profound. Figure 5b clearly shows RANS over predicts Nu by up to 4X. The results show the model transitions immediately on the SS and on the PS. Significant improvements are noted by accounting for transition, with the RANS-T predicting Nu within the experimental uncertainty at nearly every measurement point up to the transition location. The model predicts onset of transition further downstream of the data. HLES-T shows equally good agreement up to the transition location but in this case, predicts onset of transition further forward then the data. This is a good demonstration that hybrid LES modeling with a transition modeling is behaving in a physically correct way. Finally, the LES WALE results improve the transition results, but also result in higher Nu on the pressure side (PS) of the vane.

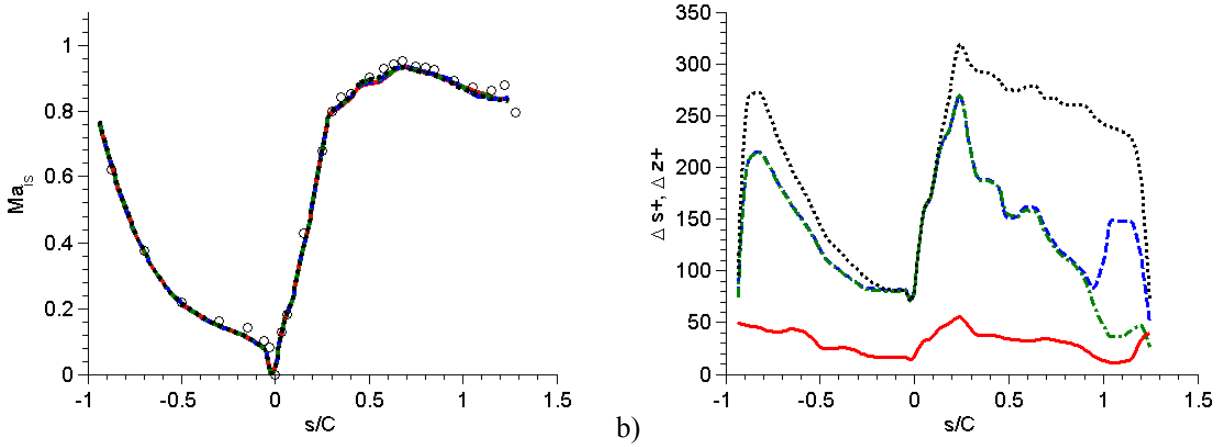

a) b)

Figure 4: Vane loading (left) and near wall Δs+ (right) for RANS (• • •), RANS-T (• – •), HLES-T (– – –), LES (——). Loading measurements (o) for Arts and Rouvroit (1992).

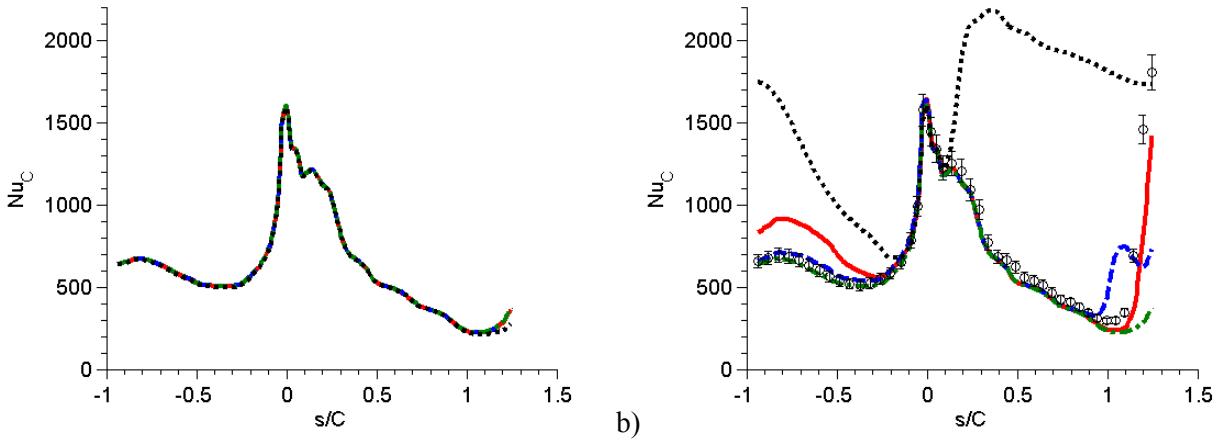

a) b)

Figure 5: Vane Nu based on chord (left) for RANS-T TI=0% (• • •), RANS-T TI=0.8%, L_e/C=5.0 (• – •), RANS-T TI=0.8%, L_e/C=0.5 (– – –), RANS-T TI=0.8%, L_e/C=0.05 (——). Vane Nu based on chord (right) for RANS (• • •), RANS-T (• – •), HLES-T (– – –), LES (——) compared to measurements (o) of Arts and Rouvroit (1992).

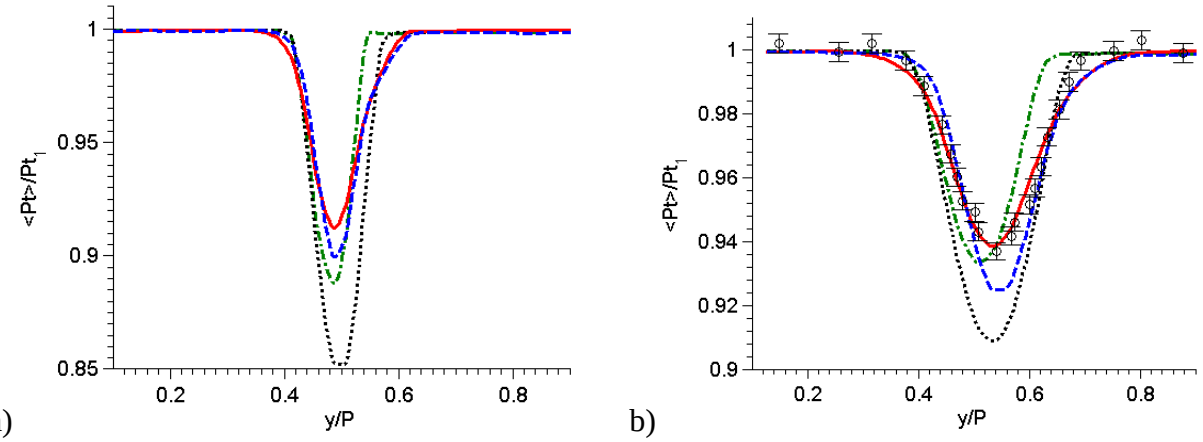

Figure 6: Vane normalized total pressure profiles at X_{VLE}/C_{AX}=1.14 (left) and X_{VLE}/C_{AX}=1.44 (right) from the vane LE for RANS (• • •), RANS-T (• – •), HLES-T (– – –), LES (——). Compared to measurements (o) of Arts and Rouvroit (1992) at X_{VLE}/C_{AX} =1.44.

Figure 6 presents total pressure results in the wake downstream normalized to the inlet (Pt1). The RANS results clearly over-predict the loss and some of that can be attributed to the boundary layer development and associated loss along the airfoil surface. At X_{VLE}/C_{AX}=1.14 the LES and HLES-T results are nearly identical, and both show good agreement with the experimental data at X_{VLE}/C_{AX}=1.44. The RANS-T results demonstrate under prediction of overall pressure loss coming off the SS surface. The under-prediction of the wake spread and over-prediction of wake depth has been well documented for RANS 2-equation models (Laskowski et al., 2015, Slotnick et al., 2014, Kopriva et al., 2013). The improved predictive capability of HLES and LES for wake mixing is critical for conditions found in the HPT.

2-D Sliding Mesh

Including the blade with a sliding mesh had little impact on the loading and heat transfer of the vane as shown in Figure 7a. Figure 7b presents Nu along the blade surface and significant differences can be observed for the different modeling approaches. Studies performed on the blade, T_{t1} is replaced with the blade's inlet relative temperature (T_{tr2}) for Equation 2. Blade alone analysis were executed for steady RANS by applying mixed out boundary conditions for momentum, enthalpy, and turbulence from the VO RANS solution (Table C3). The scale resolved simulations result in 12% higher Nu at the LE then the RANS based approaches which can be attributed to the evolution of turbulence from the vane TE to the blade leading edge and periodic unsteadiness. As with the VO simulation, the blade Nu for RANS results in earlier transition when compared with RANS-T, HLES-T and LES which predict onset of transition near s/C=0.75. A significant variation in SS heat transfer can be observed for these 3 models downstream of the transition location. On the PS surface, LES predicts the highest levels of Nu followed by HLES-T and RANS-T.

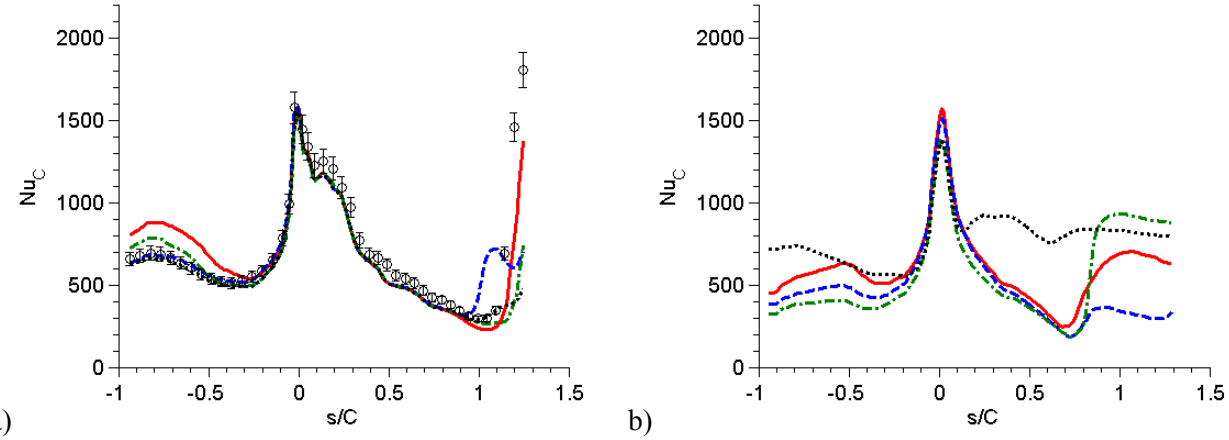

Figure 7: Vane Nu based on chord (left) for 2DSM HLES-T (• • •), 2DSM LES (• – •), VO HLES-T (– – –), VO LES (——). Compared to vane only measurements (o) of Arts and Rouvroit (1992). Blade Nu based on chord (right) for RANS (• • •), RANS-T (• – •), HLES-T (– – –), LES (——).

Figure 8a presents the blade wake total pressure normalized to the inlet (Pt1). Similar the previous section, the VO RANS and RANS-T result in a deeper wake then both the 2DSM HLES-T and LES simulations. Figure 8b presents turbulence intensity ($\sqrt{[2/3k]}/\bar{U}$) in the wake where k is the modeled kinetic energy for RANS and the resolved k ($1/2\left[u'^2+v'^2+w'^2\right]$) for HLES and LES. The velocity magnitude ($\bar{U}$) corresponds to local velocity for the vane. The resulting turbulence intensity for RANS and RANS-T are significantly below the predictions of HLES-T and LES. The impact of the downstream blade on TI outside the vane wake is near 2%, an important implication for stage simulations. This vane/blade iteration cannot be predicted for in the RANS simulations.

Figure 9a presents the blade wake relative total pressure normalized to the inlet (Ptr_2). Interestingly, the wake profile for RANS and RANS-T are nearly identical. Both simulations result in a deeper wake then both the HLES-T and LES simulations suggesting that unsteadiness plays an important role for high pressure turbine performance (Ou and Han, 1994, Didier et al., 2002, Sharma et al., 1992). Figure 9b presents turbulence intensity where $\bar{U}$ corresponds to local relative velocity for the blade. As with the relative total pressure, the resulting turbulence intensity for RANS and RANS-T are nearly identical. Like the vane, the scale resolved CFD resulted in an over a 2% increase in TI in the wake.

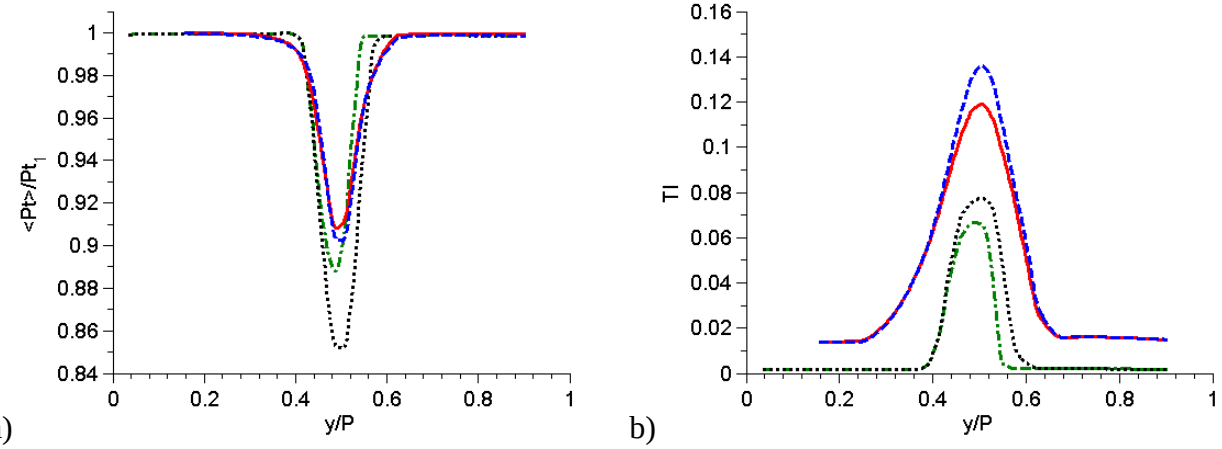

a) b)

Figure 8: Vane normalized total relative pressure (left) and local TI profiles at X_{VLE}/C_{AX} =1.14 from the blade LE for RANS (• • •), RANS-T (• – •), HLES-T (– – –), LES (——).

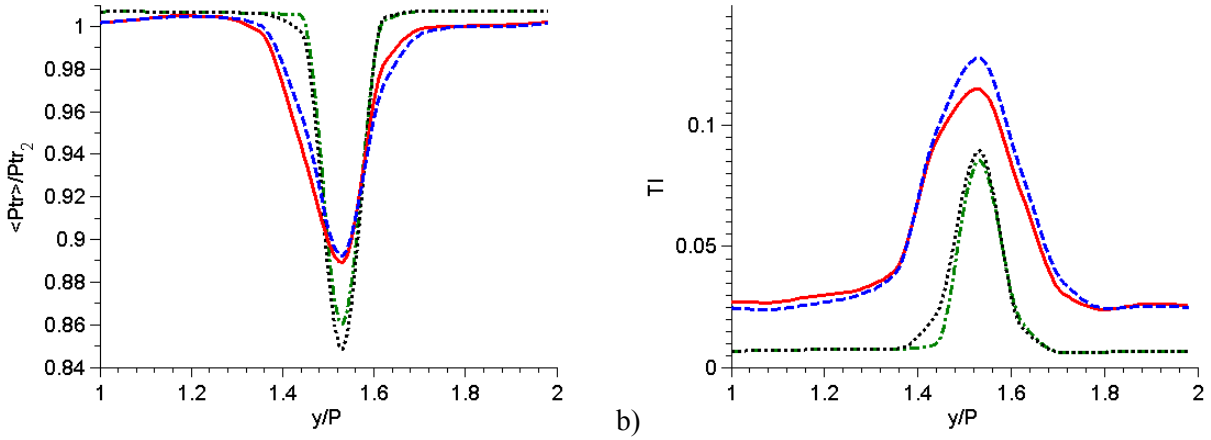

a) b)

Figure 9: Blade normalized total relative pressure (left) and local TI profiles at X_{BLE}/C_{AX} =1.17 from the blade LE for RANS (• • •), RANS-T (• – •), HLES-T (– – –), LES (——).

3-D Sliding Mesh

To reduce the computational cost for the 3D geometry, only HLES-T was run where the mesh was 2X coarser relative to the 2DSM. Figure 10 show the impact of 2X coarse mesh resolution on surface Nu for the 2DSM geometry. The mesh resolution is found to have a limited impact on the predicted vane and blade Nu where small variation is found in the region of transition on the SS surface near the TE. This provides confidence before moving to the 3DSM where the coarser mesh will have a limited impact on HLES-T predictions for the vane and downstream blade. Figure 11 presents both the loading and heat transfer along the 3D vane. Loading is found to be in good agreement across all models, where slight variation is found

near the throat. The heat transfer along the PS surface is relatively uniform on the PS for RANS-T and HLES-T. Strong differences are noted on the SS as the outer band is reached, which contributes to strong secondary flows impacting the SS heat transfer.

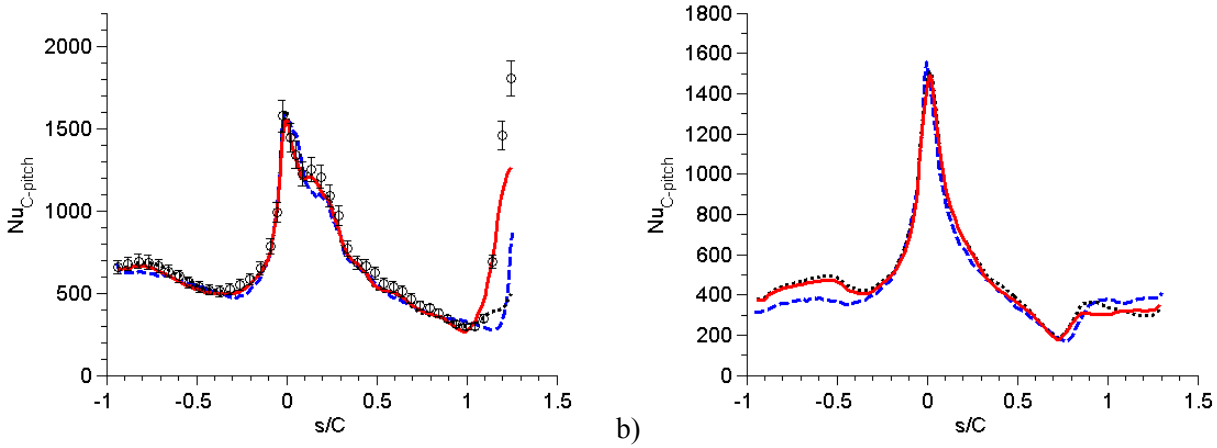

Figure 10: Vane Nu based on chord at the pitch for the vane (left) and blade (right) for coarse 3DSM (– – –), coarse 2DSM (——), and fine 2DSM (• • •) HLES-T.

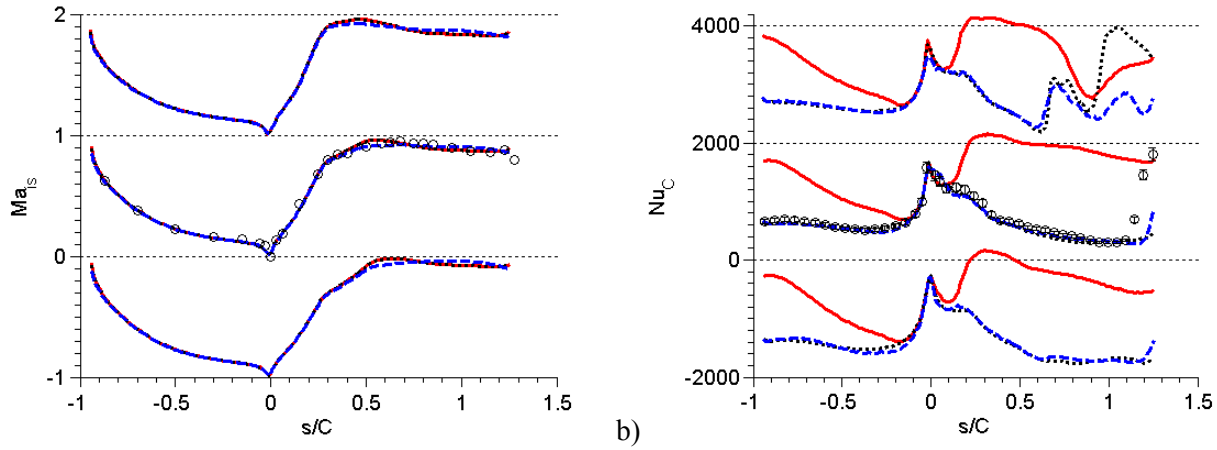

Figure 11: 3D vane loading (left) and Nu based on chord (right) for HLES-T (– – –), RANS (——), and RANS-T (• • •) at 10% (bottom), 50% (middle), and 90% (top).

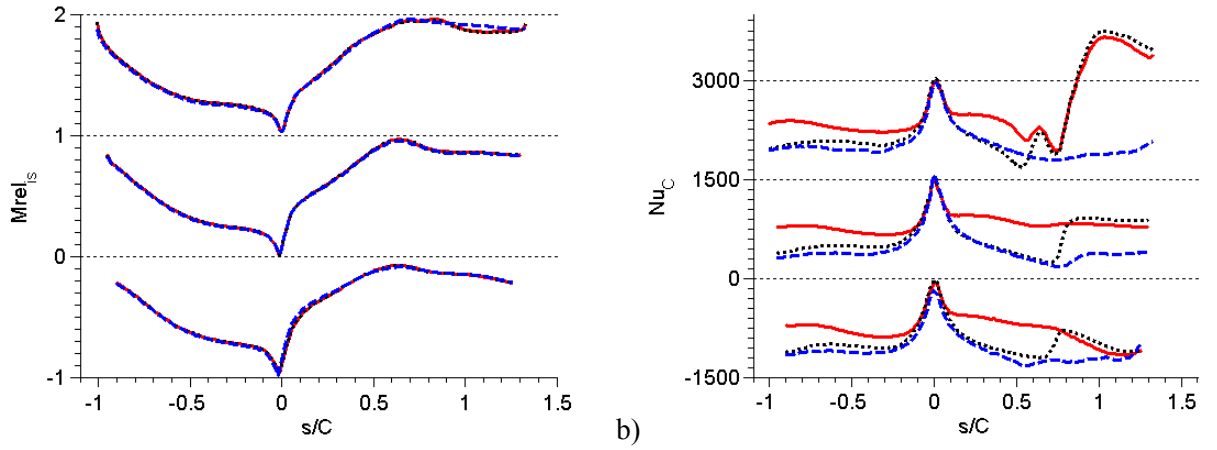

Figure 12: 3D blade loading (left) and Nu based on chord (right) for HLES-T (– – –), RANS (——), and RANS-T (• • •) at 10% (bottom), 50% (middle), and 90% (top).

Figure 12 presents both the loading and heat transfer along the 3D blade. The stagnation point is at the same location for each radial position, suggesting proper flow incidence. The loading on both the suction and pressure surface varies as a function of radius due to radial migration. The loading and heat transfer for RANS-T and HLES-T at 50% span are nearly identical, with differences noted on the SS surface near the TE.

Profound difference in Nu are found for the SS Nu where the contribution of the developing tip vortex will be discussed.

Figure 13 presents contour plots of normalized total pressure at X/C = 1.17 downstream of the TE of the blade. The total pressure is normalized based on the circumferentially averaged value at the 50% span at the inlet to be consistent with the 2D simulations discussed previously. As with the 2D simulations, the HLES-T show a wider and more mixed out wake. Figure 14 presents non-dimensional turbulent kinetic energy (TI) for the simulations at the same cut plane. Not surprisingly, high regions of TKE are associated with high regions of loss. The figures clearly show significant differences in the size, shape, location and strength of the tip vortex. RANS and RANS-T predicts the largest and strongest tip vortex, followed by HLES-T. The RANS and RANS-T simulations show the tip vortex extending 50% further into the flow-path then the HLES-T results. However, when the blade inlet TI is set to 0% the RANS-T tip vortex more closely matches the HLES-T structure. For the RANS-T simulation, it is found that the state of the boundary layer greatly impacts the "detachment" of the tip vortex from the SS surface which directly impacts the magnitude of the Nu at 90% span. Finally, instantaneous snapshots of non-dimensional total pressure show locations of where values exceed 1.0 due to energy separation (Kopriva et al., 2013). The HLES-T plots also demonstrates highly turbulent flow that can are captured on a tetrahedral unstructured mesh with a 2nd order solver.

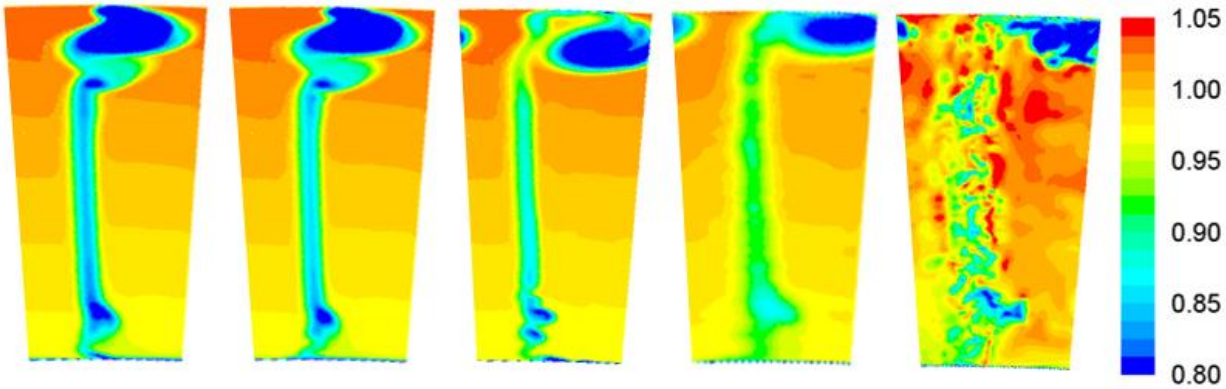

Figure 13: Normalized wake total pressure for 3D blade wake X_{BLE}/C_{AX} =1.17 for RANS, RANS-T, RANS-T (TI=0), HLES-T, and instantaneous HLES-T from left to right.

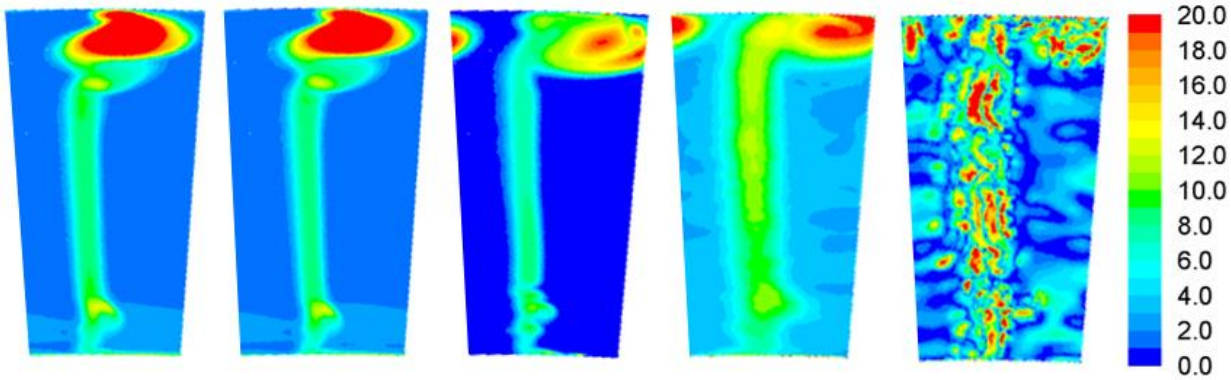

Figure 14: Local wake TI for 3D blade wake X_{BLE}/C_{AX} =1.17 for RANS, RANS-T, RANS-T (TI=0), HLES-T, and instantaneous HLES-T from left to right.

CONCLUSIONS

Numerical simulations for a transonic vane at low inlet turbulence levels have been executed on unstructured meshes for RANS, RANS with transition modeling, HLES with transition modeling and LES. The results show the importance in accounting for boundary layer transition in both wall heat transfer and downstream wake mixing. The results show promise of HLES when compared to LES for the grids considered in this study. The simulations then included a downstream blade, where blade only RANS and

RANS with transition modeling where executed with boundary conditions from the vane only RANS solution. Sliding mesh simulations for HLES with transition modeling and LES were executed. Again, significant differences were noted in wall heat transfer and wake formation downstream of the blade when accounting for transition. Finally, the 2D geometry was extended to 3D to account for endwall and tip gap effects and RANS, RANS with transition modeling for the 3D blade alone were compared to 3D simulations with sliding mesh using HLES with transition modeling. The contribution of 3D effects on the vane or blade row loss is summarized in Table 2 for HLES. Overall, significant differences were noted in wall heat transfer, tip vortex and downstream wake dynamics based on a RANS of HLES modeling approach. The results demonstrate the need for careful consideration of modeling choices when it comes to coupled versus decoupled approaches, transition, and turbulence modeling.

Table 2: Stage total relative pressure loss for 2DSM and 3DSM.

HLES-T	Vane: $1-\langle P_t\rangle/P_{t1}$	Blade: $1-\langle P_{tr}\rangle/P_{tr2}$
2DSM	1.04%	1.50%
3DSM	1.80%	3.10%

REFERENCES

Arts, T. and Rouvroit, M.L., (1992). Aero-thermal Performance of a Two-Dimensional Highly Loaded Transonic Turbine Nozzle Guide Vane: A Test Case for Inviscid and Viscous Flow Computations. Journal of Turbomachinery, 114.

Bhaskaran, R. (2010). *Large Eddy Simulation of High Pressure Turbine Cascade.* PhD dissertation, Stanford University.

Claus, R., Townsend, S., Carney, D., Horowita, J., and Turner, M. (2006). *A Case Study of High Fidelity Engine System Simulation.* 42nd AIAA/ASME/SAE/ASEE Joint Propulsion Conference

Didier, F., Denos, R., and Arts, T. (2002). *Unsteady Rotor Heat Transfer in a Transonic Turbine Stage*. Journal of Turbomachinery, 124.

Kopriva, J. E., Laskowski, G. M. and Sheikhi, M. R. H. (2015). *Hybrid LES of a High Pressure Turbine Nozzle/Blade Interaction.* DLES-10, Limassol, Cyprus.

Kopriva, J. E., Laskowski, G. M. and Shiekhi, M. R. H. (2014). Computational Assessment of Inlet Turbulence on Boundary Layer Development and Momentum/Thermal Wakes for High Pressure Turbine Nozzle and Blade. IMECE2014-38620.

Kopriva, J., Laskowski, G. M. and Shiekhi, M. R. H. (2013). Assessment of High Pressure Cooled and Uncooled Turbine Blade Wakes via RANS and URANS at Engine Scale Conditions. GT2013-94285.

Laskowski, G. M., Kopriva, J., Michelassi, V., Shankaran, S., Paliath, U., Bhaskaran, R., Wang, Q., Talnikar, C., Wang, Z. J., and Jia, F. (2016). *Future Directions of High-Fidelity CFD for Aero-Thermal Turbomachinery Research, Analysis and Design.* 46th AIAA Fluid Dynamics Conference, AIAA 2016-3322, Washington DC.

Leonard, B.P. (1991). *The ULTIMATE Conservative Difference Scheme Applied to Unsteady One-Dimensional Advection*. Comp. Methods Appl. Mech. Eng. 88, 17-74.

Mayle, R. (1991). *The Role of Laminar-Turbulent Transition in Gas Turbine Engines*. Journal of Turbomachinery. 113, 509-537.

Menter, F.R. and Langtry, R.B. and Likki, S.R. and Suzen, Y.B. and Huang, P.G. and Volker, S., (2006). *A Correlation-Based Transition Model Using Local Variables-Part I: Model Formulation*. Journal of Turbomachinery, 128, 413-422.

Morata, E. C., Gourdain, N., Duchaine, F. and Gicquel, L. Y. (2012). *Effects of free-stream turbulence on high pressure turbine heat transfer predicted by structured and unstructured LES.* Int. Journal of Heat and Mass Transfer, vol. 55, pp 21-22.

Nicoud, F. and Ducros, F., (1999). *Subgrid-scale Stress Modeling Based on the Square of the Velocity Gradient Tensor*. Flow, Turbulence, and Combustion, 62, 183-200.

Ou, S., and Han, J.C. (1994). Unsteady Wake Effect on Film Effectiveness and Heat Transfer Coefficient from a Turbine Blade with One Row of Air and CO2 Film Injection. Journal of Turbomachinery.

Sharma, O.P., Pickett, G.F., and Ni, R.H. (1992). *Assessment of Unsteady Flows in Turbines.* Journal of Turbomachinery, 114.

Shur, M.L. and Spalart, P.R. and Strelets, M.K. and Travin, A.K. (2008). *A Hybrid RANS-LES Approach with Delayed-DES and Wall-Modelled LES Capabilities.* International Journal of Heat and Fluid Flow, 29, 1638-1649.

Slotnick, J. and Khodadoust, A. and Alonso, J. Darmofal, D. and Gropp, W. and Lurie, E. and Mavriplis, D., (2014). *CFD Vision 2030 Study: A Path to Revolutionary Computational Aerosciences.* NASA Tech. Report, 218178.

Stock, H.W. and Haase, W. (2006). *Navier-Stokes Airfoil Computations with eN Transition Prediction Including Transitional Flow Regions*. AIAA Journal. 38, 2059-2066.

Tinoco, E.N., Bogue, D.R., Kao, T.-J., Yu, N.J., Li, P. and Ball, D.N. (2005). *Progress Toward CFD for Full Flight Envelope*. The Aeronautical Journal. 109.

Walker, G.J., (1993). The Role of Laminar-Turbulent Transition in Gas Turbine Engines: A Discussion. Journal of Turbomachinery. 115, 207-216.

Zlatinov, M. and Laskowski, G., (2015). Hybrid Large-Eddy Simulation Optimization of a Fundamental Turbine Blade Turbulated Cooling Passage. Journal of Propulsion and Power, 31, 1292-1297.

APPENDIX

Table A: Domain Summary.

2DVO	2-D Extruded Vane Only
2DBO	2-D Extruded Blade Only
2DSM	2-D Extruded Linear Sliding Mesh
3DVO	3-D Center-line Vane Only
3DBO	3-D Center-line Blade Only
3DSM	3-D Center-line Sliding Mesh

Table B: Geometry Summary.

Geometry	***2D***	***3D***
Vane C_{ax} [mm]	36.8	36.8
Blade C_{ax} [mm]	30.6	30.6
Stage Gap [mm]	13.6	13.6
Blade Tip Gap [mm]	N/A	0.508
Airfoil Fillet Radius [mm]	N/A	1.016
Passage Height [mm]	N/A	50.8

Table C1: Vane Only Boundary Conditions.

Vane	***2DVO***	***3DVO***
Pt_1 [kPa]	184.9	184.9
Tt_1 [K]	409	409
Inlet Flow [deg]	0	0
T_{wall} [K]	300	300
Ps_2 [kPa]	116.5	3DSM 1D Radial Profile (Avg=115)
k [m^2/s^2] (RANS)	0.34	0.34
ω [1/s] (RANS)	355	355

Table C2: Blade Only RANS and RANS-T Boundary Conditions.

Blade	***2DBO***	***3DBO***
Ptr_2 [kPa]	2DVO (122)	3DVO 1D Radial Profile (Avg=121.2)
Ttr_2 [K]	2DVO (363)	3DVO 1D Radial Profile (Avg=363)
Inlet Flow [deg]	2DVO (33.4)	3DVO 1D Radial Profile (Avg=30.8
k [m^2/s^2]	2DVO (50)	3DVO 1D Radial Profile (Avg=59)
ω [1/s]	2DVO (2.9E5)	3DVO 1D Radial Profile (Avg=2.9E5)
T_{wall} [K]	300	300
Ps_3 [kPa]	78.6	78.6

Table C3: Sliding Mesh LES and HLES Boundary Conditions.

Sliding Mesh	***2DSM***	***3DSM***
Pt_1 [kPa]	184.9	184.9
Tt_1 [K]	409	409
Inlet Flow	Axial	Axial
T_{wall} [K]	300	300
Ps_3 [kPa]	78.6	78.6
Blade Speed	250 [m/s]	683 [rad/s]

Table D: 2DSM (PBD02) and 3DSM (CBD02) Blade Coordinates [mm].

2DSM		***3DSM (90%Span)***			***3DSM (50%Span)***			***3DSM (10%Span)***		
X	**Y**	**X**	**Y**	**Z**	**X**	**Y**	**Z**	**X**	**Y**	**Z**
80.56	-31.52	79.15	-47.76	383.42	79.34	-44.74	363.32	80.57	-42.77	343.09
80.09	-32.73	78.15	-49.78	383.16	78.69	-45.85	363.18	80.09	-43.96	342.94
79.41	-34.47	76.47	-52.93	382.74	77.86	-47.23	363.01	79.42	-45.60	342.72
78.25	-37.34	74.40	-56.33	382.26	76.71	-49.07	362.76	78.54	-47.68	342.44
76.81	-40.79	72.26	-59.23	381.82	74.98	-51.65	362.40	77.35	-50.35	342.06
75.20	-44.54	69.18	-62.45	381.31	72.45	-54.94	361.92	75.70	-53.77	341.54
73.45	-48.32	66.26	-64.62	380.94	69.07	-58.40	361.38	73.52	-57.80	340.88
71.54	-51.97	63.10	-66.30	380.65	65.57	-60.92	360.96	71.30	-61.34	340.26
69.49	-55.29	59.86	-67.59	380.43	61.36	-62.88	360.62	68.46	-64.93	339.59
66.87	-58.23	56.69	-68.71	380.23	57.29	-64.07	360.41	65.32	-67.60	339.07
63.63	-60.24	53.29	-69.96	380.00	53.69	-64.95	360.26	61.01	-69.29	338.73
59.79	-61.06	50.64	-71.86	379.64	50.73	-66.50	359.97	56.84	-69.03	338.78
55.78	-60.33	51.54	-75.29	378.98	51.27	-70.09	359.29	53.42	-67.28	339.13
53.18	-58.72	54.75	-77.71	378.49	53.66	-72.48	358.82	51.11	-64.60	339.66
51.39	-56.71	57.95	-78.73	378.28	57.26	-74.14	358.48	50.64	-61.27	340.27
50.43	-54.29	61.31	-78.71	378.28	61.14	-74.35	358.43	53.58	-59.31	340.62
51.84	-51.96	64.67	-77.53	378.53	64.80	-73.12	358.69	57.54	-58.54	340.75
54.40	-51.17	67.77	-75.14	379.01	68.23	-70.34	359.24	62.02	-57.46	340.94
57.60	-50.44	70.15	-72.15	379.59	70.87	-66.72	359.93	65.93	-55.84	341.21
61.62	-49.24	72.11	-68.76	380.22	72.88	-63.09	360.59	69.73	-53.38	341.60
65.73	-47.36	73.69	-65.43	380.81	74.68	-59.37	361.22	72.72	-50.62	342.02
69.33	-44.66	75.07	-62.20	381.35	76.65	-54.97	361.91	75.04	-47.94	342.41
72.34	-41.46	76.67	-58.21	381.98	78.03	-51.69	362.40	76.69	-45.79	342.70
74.76	-38.35	78.16	-54.32	382.55	78.99	-49.32	362.73	77.91	-44.11	342.92
76.81	-35.24	79.48	-50.77	383.03	79.73	-47.44	362.98	78.81	-42.86	343.08
78.08	-33.09	80.32	-48.47	383.33	80.29	-46.02	363.16	79.49	-41.88	343.20
78.94	-31.61	80.88	-46.95	383.52	80.71	-44.92	363.30	79.82	-41.42	343.25
79.53	-30.57	80.91	-46.87	383.53	80.91	-44.40	363.36			